Data-Driven Output Prediction and Efficiency Optimization Control for Wireless Power Transfer Systems

Fei Xu, *Member, IEEE*, Xiquan Deng, Zhixin Chen, *Graduate Student Member, IEEE*, Xian Zhang, and Chi K. Tse, *Fellow, IEEE*

***Abstract*—Existing research on efficiency optimization for wireless power transfer (WPT) systems is limited by complicated models and low control accuracy. In this article, a data-driven efficiency optimization control method is proposed for phase-shift controlled WPT systems. This method integrates an experimental data-driven output prediction and efficiency optimization approach, driven by a multilayer perceptron (MLP) and particle swarm optimization (PSO). First, the MLP model establishes a nonlinear mapping between phase shift angles and key performance indicators, including output power and system efficiency. Subsequently, the PSO algorithm determines the optimal phase angle combination that maximizes efficiency for a given reference power. In addition, the PSO-generated control parameters are regressed using lightweight artificial neural networks, enabling real-time deployment onto microcontrollers. To verify the accuracy of the proposed data-driven efficiency optimization control WPT method with MLP and PSO, an experimental 430 W/85 kHz prototype is built. The measured results show that the mean absolute percentage error of the MLP predictive model is less than 3.5% across all selected load conditions. Meanwhile, the efficiency tracking algorithm driven by PSO ensures high-efficiency operation under variation of the reference power, load resistance, and mutual inductance with a maximum efficiency of 93.5%.**

***Index Terms*—Data-driven methods, efficiency optimization, output prediction, wireless power transfer (WPT).**

I. Introduction

WIRELESS power transfer (WPT) technology has revolutionized the way energy is delivered, providing a contactless power transfer solution for diverse applications such as electric vehicles [1], [2], [3], autonomous underwater vehicles [4], [5], [6], and consumer electronics [7]. In these applications, maintaining stable and high-efficiency power transfer is crucial for ensuring reliable operation.

However, accurately modeling and optimizing WPT systems remains a significant challenge. The power transfer characteristics of WPT systems are inherently nonlinear and strongly influenced by circuit parameters and operating conditions [8], [9]. In particular, variations in load resistance R_{L}, caused by dynamic power demand or battery state-of-charge fluctuations, introduce significant uncertainty in system output, making it difficult to maintain stable power delivery and high efficiency. Conventional analytical models attempt to predict these variations, but often struggle to generalize across diverse operating conditions, leading to discrepancies between theoretical predictions and real-world performance.

Existing research on WPT systems predominantly relies on theoretical modeling approaches. One widely used method is fundamental harmonic approximation (FHA) [10], [11], [12], which simplifies system analysis by considering only the fundamental frequency component while neglecting higher-order harmonics. While FHA provides a computationally efficient analytical framework, it inherently assumes a linearized operating condition and neglects nonlinear circuit behaviors, such as high-order harmonics [13] and switching effects [14]. As a result, its accuracy deteriorates under varying load conditions and high-frequency switching environments.

To address these limitations, recent studies have sought to refine traditional models. For instance, refined ac resistance models have been developed to incorporate rectifier bridge discontinuities, improving the precision of output power predictions in practical applications [15], [16]. In addition, other approaches integrate switching losses and parasitic effects into the modeling framework to enhance accuracy [17]. Further advancements include dynamic models based on switching states [18], which leverage transient characteristics of primary current and capacitor voltage to establish state-triggered rules and enhance system performance across diverse conditions. Although these refinements improve modeling accuracy, they often introduce significant computational complexity, making real-time optimization and control challenging.

The fundamental tradeoff between model accuracy and computational efficiency would therefore limits the practical

Received 29 January 2025; revised 21 April 2025; accepted 20 May 2025. Date of publication 26 May 2025; date of current version 5 August 2025. This work was supported in part by China National Foundation Project under Grant 52407004, in part by China National Foundation Project under Grant 52477005, and in part by Hong Kong RGC GRF under Grant 11205222, and in part by Hebei Province Yout Talent Program under Grant BJK2024059. Recommended for publication by Associate Editor O. L. Lucia. *(Corresponding author: Xian Zhang.)*

Fei Xu, Xiquan Deng, Zhixin Chen, and Xian Zhang are with the State Key Laboratory of Intelligent Power Distribution Equipment and System, Hebei University of Technology, Tianjin 300130, China (e-mail: feify.xu@connect.polyu.hk; 202321401047@hebut.edu.cn; zhixinchen@ieee.org; zhangxian@hebut.edu.cn).

Chi K. Tse is with the Department of Electrical Engineering, City University of Hong Kong, Kowloon, Hong Kong (e-mail: cktse@ieee.org).

This article has supplementary material provided by the authors and color versions of one or more figures available at https://doi.org/10.1109/TPEL.2025.3573712.

Digital Object Identifier 10.1109/TPEL.2025.3573712

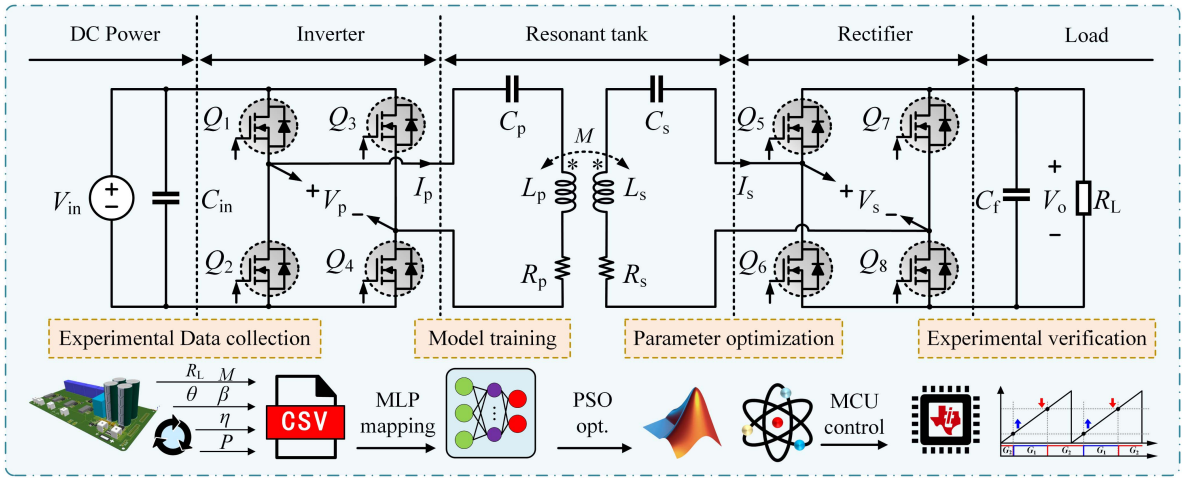

Fig. 1. Overview of the proposed data-driven control methodology for WPT systems.

applicability of traditional methods. This necessitates an alternative approach that can achieve high prediction accuracy while maintaining computational efficiency, enabling real-time optimization of WPT systems. Conventional optimization methods also suffer from suboptimal performance due to their reliance on static models. Most existing approaches determine control parameters, such as phase shift angles (β, θ), based on theoretical models that do not adapt to variations in R_{L}. As a result, these methods yield solutions that are only optimal under nominal conditions but fail to maintain efficiency when the system deviates from ideal assumptions [19]. A more adaptive approach is required—one that learns from experimental data to capture the nonlinear dependencies between system parameters and dynamically adjust control variables in real time. The proposed solution, data-driven efficiency optimization control-WPT, leverages data-driven methodologies to dynamically adjust phase shift angles (β, θ) based on real-time load variations, thus enabling a more adaptive and efficient control strategy compared to conventional methods.

To achieve this, researchers have explored AI-driven techniques in power electronic converters, particularly in converters modulation and control strategies. Machine learning methods have been applied to modulation control [20] and current stress minimization [21]. However, these studies are often constrained by their dependence on simplified simulation models or inaccurate loss calculations, which may limit their effectiveness in real-world implementations.

In the WPT domain, AI has primarily been used for parameter identification [22] and coil design optimization [23], rather than real-time control. Despite these advancements, the application of AI for efficiency optimization and power regulation in WPT systems remains largely unexplored. This study aims to bridge this gap by proposing an efficiency optimization control for WPT method through leveraging a data-driven methodology to dynamically adjust phase shift angles (β, θ) based on real-time load variations, offering a more adaptive and efficient control solution.

This study investigates the use of data-driven approaches to optimize WPT systems under diverse operational conditions. Compared with theoretical models that often oversimplify system behavior, data-driven efficiency optimization control-WPT leverages historical system data to adaptively refine predictions and enhance real-world applicability. By employing multilayer perceptrons (MLPs) for nonlinear mapping and particle swarm optimization (PSO) for tuning optimal parameters, this approach addresses both modeling inaccuracies and optimization challenges. To enable real-time execution, the PSO-optimized control surfaces are further regressed using lightweight artificial neural network (ANN), which are deployed on a TMS320F28335 DSP. Furthermore, integrating experimental data ensures a closer alignment between the model and real-world scenarios, as illustrated in Fig. 1.

To validate the proposed data-driven efficiency optimization control-WPT methodology, this study focuses on a specific example of maintaining constant power (CP) output. Experimental results demonstrate the feasibility of achieving high-precision control and adaptability to varying conditions.

The rest of this article is organized as follows. Section II elaborates on the operating principles of WPT systems and establishes the limitations of conventional constant power output modeling. Section III introduces the proposed data-driven framework, and Section IV validates its performance through experimental results. Section V extends the analysis to cover coupling variation and generalization under misalignment. Finally, Section VI concludes this article.

II. System Operation and Model Limitations

In this section, we introduce the basic operating principles of WPT systems and discuss the limitations of output models.

A. Operating Principles of Phase-Shift WPT Systems

A WPT system typically consists of an inverter, a compensation network, coupled coils, a rectifier and a load, as shown in Fig. 1. On the primary side, the system includes a dc power source V_{in}, a primary inverter (H-bridge with switches Q_1 to Q_4), and a resonant tank comprising a series capacitor C_{p} and the primary coil L_{p}. Energy is transferred wirelessly through the

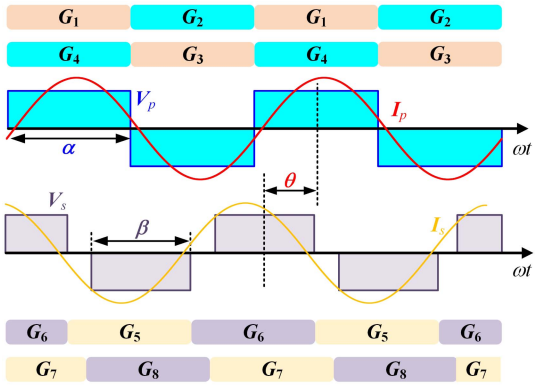

Fig. 2. Typical steady-state control signals G_1 to G_8 and H-bridges corresponding waveforms V_p, V_s, I_p, and I_s.

coupled coils, which act as a loosely coupled transformer. When alternating current flows through the primary coil L_p, it generates a time-varying magnetic field. This magnetic field induces a voltage in the secondary coil L_s due to mutual inductance M, where the coupling coefficient k defines the strength of the magnetic linkage between the coils. The secondary side consists of a secondary series capacitor C_s, a secondary active rectifier (H-bridge with switches Q_5 to Q_8), a filter capacitor C_f, and an equivalent load resistor R representing the battery. The rectifier converts the induced ac voltage into dc voltage to power the load. The system is operated at a fixed resonant frequency of 85 kHz. To minimize reactive power circulation, a compensation network is employed, with its resonant frequency set to match the system's operating frequency. This ensures that the compensation network reduces reactive losses by maintaining resonance, thus improving overall system efficiency.

The control signals G_1 to G_8 play a crucial role in controlling the switches Q_1 to Q_8, as shown in Fig. 2. These signals define the operation of the primary and secondary bridges in the WPT system. Specifically, on the primary side, G_1 and G_2 control the half-bridge switches Q_1 and Q_2, while G_3 and G_4 control Q_3 and Q_4, completing the primary bridge. Similarly, G_5 to G_8 control the secondary half-bridge switches Q_5 to Q_8. These gate signals are complementary square waves, alternating within each half-bridge with a small dead time to prevent simultaneous conduction, ensuring the safe operation of the full-bridge inverter and rectifier.

By modulating these control signals, the system achieves phase shift modulation, which involves three critical control parameters, namely, α, β, and θ. The phase shift angles α, β, and θ are essential in determining the power transfer characteristics of WPT systems. The conduction angles α and β represent the phase overlap of the control signals within the primary and secondary bridges, respectively. These angles determine the duration of simultaneous switch conduction. The relative phase angle θ, defined as the phase difference between the voltage waveforms V_p and V_s, adjusts the overlap of primary and secondary voltages. In this study, the phase shift angle α is fixed, and the two phase shift angles on the secondary side: θ and β are to be optimized. Specifically, the focus is on tuning the secondary side's phase shift angles (θ, β) to optimize power transfer efficiency.

B. Discrepancies Between Theoretical Predictions Versus Experimental Observations

In WPT systems, accurate output power prediction and efficiency estimation are fundamental for performance optimization. However, discrepancies often arise between theoretical models and experimental measurements, making the application of these models in real-world scenarios challenging.

The theoretical output power P_o of the system [17] is given by

$$P_\mathrm{o} = \frac{8V_\mathrm{in}V_\mathrm{o}}{\pi^2\omega M}\sin\left(\frac{\beta}{2}\right)\sin(\theta) \tag{1}$$

where V_in and V_o represent the input and output voltages, ω is the resonant angular frequency ($\omega = 2\pi f$), and M is the mutual inductance between the coupled coils.

The theoretical efficiency η of the system is derived as

$$\begin{aligned}\eta &= \frac{I_\mathrm{s}^2 R_\mathrm{eq}}{I_\mathrm{s}^2 R_\mathrm{eq} + I_\mathrm{s}^2 R_\mathrm{s} + I_\mathrm{p}^2 R_\mathrm{p}} \\ &= \frac{\omega M \sin\theta}{\omega M \sin\theta + K R_\mathrm{p} + \frac{1}{K} R_\mathrm{s}}\end{aligned} \tag{2}$$

where R_eq is the equivalent load resistance, R_s is the resistance of the secondary-side coil, and R_p is the resistance of the primary-side coil. The constant K is defined as

$$K = \frac{I_\mathrm{p}}{I_\mathrm{s}} = \frac{V_\mathrm{o}\sin\frac{\beta}{2}}{V_\mathrm{in}}. \tag{3}$$

It should be noted that while these equations provide a theoretical foundation for output power and efficiency, they often rely on simplified assumptions, such as ideal components and neglecting higher-order harmonics. These assumptions lead to significant discrepancies when compared to experimental results, making the models less reliable for real-world applications.

As shown in Fig. 3, the variation of output power P_o with phase shift angle β is illustrated. Under operating conditions of $R = 45\,\Omega$ and $\theta = 90°$, a noticeable discrepancy is observed between theoretical predictions and experimental measurements. The relative error can reach up to 24.9%, highlighting the limitations of conventional models. To quantify the deviation between prediction and measurement, the following metric is used:

$$\xi = \left|\frac{y_\mathrm{theor} - y_\mathrm{meas}}{y_\mathrm{meas}}\right| \tag{4}$$

where y represents the target variable, e.g., P_o or η.

These discrepancies not only hinder the system's ability to maintain stable outputs, but also compromise its efficiency and reliability. The limitations of conventional models arise from their reliance on static assumptions that fail to capture the nonlinear behaviors of WPT systems in practical conditions. This underscores the need for advanced, adaptive modeling, and optimization approaches that can better reflect the system's dynamics under practical operating conditions. These limitations

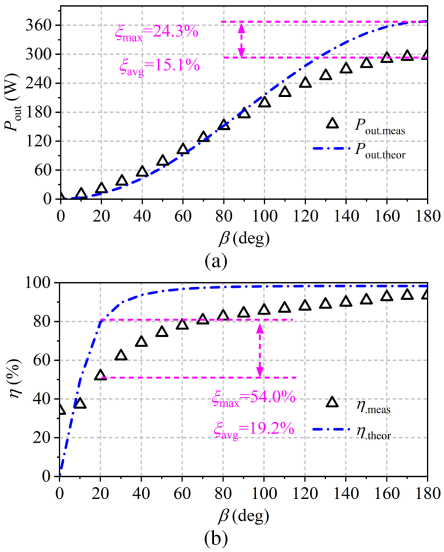

Fig. 3. Comparison of theoretical and measured results with respect to β: (a) output power and (b) power efficiency.

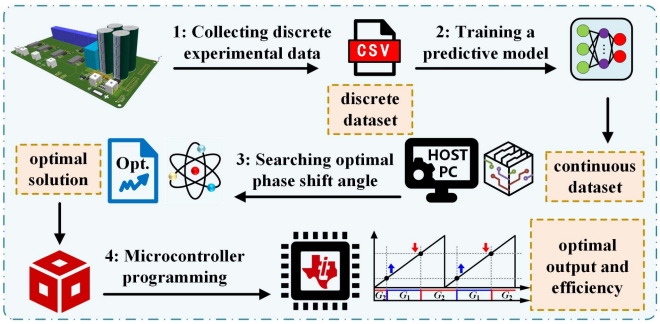

Fig. 4. Workflow of the proposed data-driven efficiency optimization control for WPT systems.

motivate the use of data-driven modeling and control methods, as introduced in the following section.

III. Proposed Data-Driven Methodology

This study introduces a data-driven efficiency optimization control-WPT methodology aimed at overcoming the limitations of conventional modeling and optimization techniques in WPT systems. By leveraging historical experimental data, this approach employs MLP for mapping-based modeling and PSO for searching optimal parameter solutions. This methodology enables accurate predictions of key performance metrics, such as η and P_o, while adapting to variations in load resistance R_L, mutual inductance M, and target output P_{ref} demands. The workflow of the proposed data-driven efficiency optimization control-WPT methodology is illustrated in Fig. 4.

The data-driven efficiency optimization control-WPT framework follows a comprehensive, end-to-end process that bridges the gap between theoretical models and real-world implementation, addressing the inherent nonlinearities and complexities in

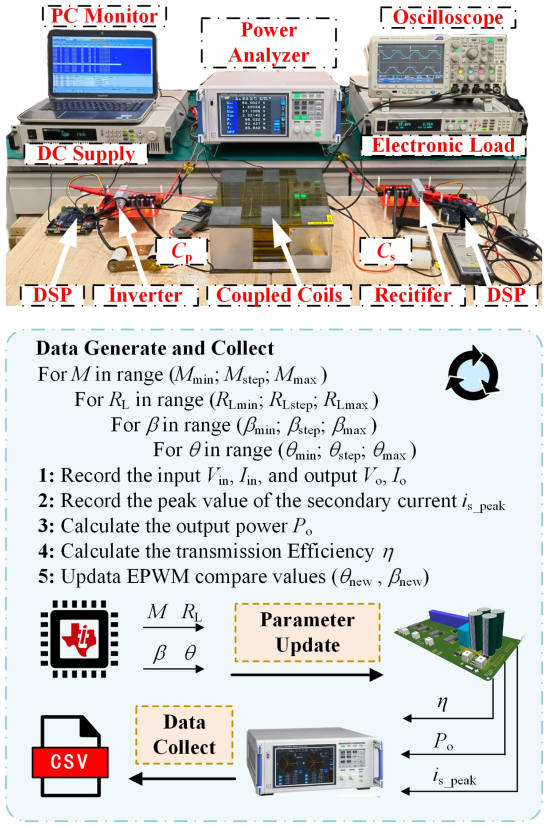

Fig. 5. Data acquisition process for the WPT system.

WPT systems. The following sections will provide a detailed explanation of each stage, including experimental data collection, modeling techniques, and optimization strategies employed in data-driven efficiency optimization control-WPT.

A. Experimental Setup and Data Collection

An experimental platform was developed to collect data supporting the proposed data-driven efficiency optimization control methodology for WPT systems. The platform consists of a primary and secondary coil, a compensation network, and a control circuit. A Digital Signal Processor (DSP)-based microcontroller was employed to implement optimized control parameters and manage real-time system operations. A photograph of the experimental prototype is shown in Fig. 5, and its key parameters are summarized in Table I.

Data for this study were collected using the custom-built WPT prototype system. As shown in Fig. 5, the data acquisition process was designed to ensure accuracy and repeatability by precisely controlling system parameters and employing high-speed automated measurements.

A DSP-based microcontroller generated control signals for the phase shift angle β and relative phase θ, which were cyclically updated through controller area network communication. These parameters were adjusted iteratively to explore the operating space of the system. In addition, a HIOKI PW6001 power analyzer was used to measure the dc input voltage V_{in},

TABLE I
KEY PARAMETERS OF THE WPT PROTOTYPE

Parameter	Symbol	Value
Rated charging power	P_{o}	0–430 W
Input voltage	V_{in}	50 V
Switching frequency	f	85 kHz
MOSFETs	$Q_1 - Q_8$	IPW60R060P7
Preliminary inductance	L_{p}	146.1 μH
Secondary inductance	L_{s}	144.2 μH
Mutual inductance	M	20.98 to 28.46 μH
Coil resistances	R_p, R_s	0.121 Ω, 0.124 Ω
Compensation capacitances	C_{p}, C_{s}	24 nF, 24.3 nF

dc input current I_{in}, dc output voltage V_{o}, and dc output current I_{o}. This automated data acquisition process minimized human intervention, ensuring reliable and consistent data collection.

To ensure the dataset covers coupling variation, the receiver coil was laterally displaced across 6 offset positions (from 0 to 10 cm in 2-cm steps), each corresponding to a different mutual inductance M. For every displacement setting, the control parameter sweep was repeated to ensure uniform sampling coverage.

The output power P_{o} and system efficiency η were calculated as

$$P_{\mathrm{o}} = V_{\mathrm{o}} \cdot I_{\mathrm{o}}, \tag{5}$$

$$\eta = \frac{P_{\mathrm{o}}}{V_{\mathrm{in}} \cdot I_{\mathrm{in}}}. \tag{6}$$

To improve model generalization, the full dataset was normalized using min-max scaling and split into training (70%), validation (20%), and testing (10%) subsets. The parameter space was systematically explored by varying β from 10° to 180° in 10° steps, θ from 10° to 90°, and R_{L} from 15 to 45 Ω. This yielded a total of $18 \times 9 \times 7 \times 6 = 6804$ operating points.

In addition, the peak value of the secondary-side current, i_{s_peak}, was recorded for each operating point. As discussed in [19], mutual inductance M can be approximated as

$$M \approx \frac{4V_{\mathrm{in}}}{\pi \omega i_{s\_peak}} \tag{7}$$

indicating that i_{s_peak} serves as an effective observable reflecting coupling strength. Rather than measuring M directly, the data-driven model uses i_{s_peak} as an input feature, avoiding analytical simplifications, and enhancing robustness across varying system conditions.

B. Data-Driven Output Prediction Modeling: MLP

Machine learning algorithms, particularly MLP, were chosen for the task of predicting system efficiency η and output power P_{o} due to their ability to model complex nonlinear relationships between input and output parameters. Unlike traditional mathematical models, which often rely on simplified assumptions and fail to capture the intricate interactions of real-world systems, MLPs can learn directly from experimental data, making them ideal for capturing the complex behavior of the WPT system under varying operational conditions, including changes in mutual inductance due to misalignment.

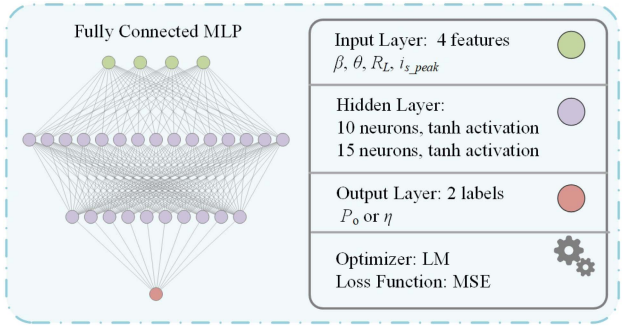

Fig. 6. Architecture of the fully connected MLP for predicting output power and system efficiency.

In this study, two independent MLP models have been developed to predict system efficiency η and output power P_{o}, respectively. By decoupling these outputs, each MLP would extract the relevant features and improve predictive accuracy. The trained MLP models enable real-time predictions of P_{o} and η, which serve as the foundation for optimizing the WPT system.

As illustrated in Fig. 6, each MLP consists of an input layer, two hidden layers, and an output layer. The input layer contains four neurons representing θ, β, R_{L}, and i_{s_peak}, which together define the system's operational state and coupling condition. This design allows each model to focus on a single target, avoiding interference between outputs during training. To determine the optimal network architecture, an ablation study is conducted, evaluating multiple configurations with different numbers of neurons. The tanh activation function is employed in the hidden layers to introduce nonlinearity while preventing gradient vanishing. The output layer consists of a single neuron with a linear activation function, ensuring continuous-valued predictions for P_{o} and η.

The relationship between the input parameters and the predicted outputs can be expressed as

$$\hat{y}_i = f_i(\theta, \beta, R_{\mathrm{L}}, i_{s\_peak}) + \epsilon_i, \quad i \in \{1, 2\} \tag{8}$$

where $f_1(\theta, \beta, R_{\mathrm{L}}, i_{s\_peak})$ represents the mapping function for P_{o}, $f_2(\theta, \beta, R_{\mathrm{L}}, i_{s\_peak})$ represents the mapping function for η, and ϵ_i accounts for modeling errors.

The training process is formulated as an optimization problem, where the mean squared error (MSE) is minimized, i.e.,

$$\mathcal{L}_{\mathrm{MLP}} = \frac{1}{N} \sum_{i=1}^{N} (\hat{y}_i - y_i)^2 \tag{9}$$

where N is the number of training samples, $\hat{y}_i$ is the predicted value, and y_i is the ground truth. The dataset is divided into 70% training, 20% validation, and 10% testing to ensure generalization.

To update the model parameters, the Levenberg–Marquardt (LM) optimization algorithm is employed. This method iteratively updates the network weights $\boldsymbol{W}$ and biases $\boldsymbol{b}$ by approximating the Hessian matrix using the Jacobian of the network errors. At iteration j, the parameter update rule is given by

$$\Delta \boldsymbol{w}^{(j)} = -\left(\boldsymbol{J}^T\boldsymbol{J} + \mu \boldsymbol{I}\right)^{-1}\boldsymbol{J}^T\boldsymbol{e} \tag{10}$$

where $\boldsymbol{J}$ is the Jacobian matrix of partial derivatives of the network errors with respect to the parameters, μ is the damping factor that controls the step size, and $\boldsymbol{e}$ is the vector of prediction errors.

The network parameters are then updated as

$$\boldsymbol{w}^{(j+1)} = \boldsymbol{w}^{(j)} + \Delta \boldsymbol{w}^{(j)}. \tag{11}$$

Here, $\boldsymbol{w}$ includes all trainable parameters in the network, including both weights and biases. The LM algorithm combines the advantages of gradient descent and the Gauss–Newton method, enabling fast convergence for small to medium-sized networks.

The trained MLP model is integrated into the overall optimization framework to guide the parameter selection process. Since WPT systems require optimal θ and β to maximize efficiency and regulate output power, a direct analytical mapping is often impractical. Instead, the MLP model enables rapid and accurate function approximation, replacing computationally expensive simulations. The predicted P_{o} and η values serve as objective functions for the subsequent PSO process, ensuring that the system operates under optimal conditions.

To enhance reproducibility and facilitate external validation, the dataset used for model training, along with the trained MLP model parameters and the code of the optimization framework, have been included as supplementary materials.

C. Searching Optimal Solution Using PSO

The optimization is carried out for each operating condition defined by the load resistance R_{L}, mutual inductance M, and target output power P_{ref}, with the goal of identifying the optimal control angles (θ, β). The primary objective of the optimization is to maximize system efficiency η while ensuring that the output power P_{o} remains within an acceptable range around the reference value P_{ref}. The optimization problem is formulated as

$$\max_{\beta,\theta} \eta^{(i)} \quad \text{subject to} \quad |P_{\mathrm{o}}^{(i)} - P_{\mathrm{ref}}^{(i)}| \le \Delta P \tag{12}$$

where β and θ are the phase shift angles to be optimized for the ith operating condition, and ΔP defines the allowable deviation for power output.

To incorporate this constraint into the optimization process, the problem is expressed as a composite loss function that jointly penalizes power deviation and rewards efficiency

$$\min_{\beta,\theta} \mathcal{L}_{\mathrm{PSO}}^{(i)} = \lambda_1 \left(P_{\mathrm{o}}^{(i)} - P_{\mathrm{ref}}^{(i)}\right)^2 - \lambda_2 \eta^{(i)} \tag{13}$$

where λ_1 ensures compliance with the power constraint, while λ_2 prioritizes efficiency.

To solve this optimization problem efficiently, we use the PSO algorithm, which iteratively updates each particle's velocity and position

$$\boldsymbol{v}_i(t+1) = \omega_{\mathrm{p}}\boldsymbol{v}_i(t) + c_1 r_1(\boldsymbol{p}_i - \boldsymbol{x}_i) + c_2 r_2(\boldsymbol{g} - \boldsymbol{x}_i), \tag{14}$$

$$\boldsymbol{x}_i(t+1) = \boldsymbol{x}_i(t) + \boldsymbol{v}_i(t+1) \tag{15}$$

where $\boldsymbol{v}_i(t)$ and $\boldsymbol{x}_i(t)$ represent the velocity and position of the ith particle at iteration t. The parameters ω_{p}, c_1, and c_2 control the exploration and exploitation balance, with r_1 and r_2 sampled from $[0, 1]$.

The PSO process continues to iterate until a stopping criterion is met, such as reaching the maximum number of iterations or achieving an acceptable loss function value. As shown in Fig. 7, PSO begins with extensive global exploration in the early stages, allowing particles to search broadly throughout the solution space. As iterations progress, the algorithm transitions to fine-tuned local search, enabling particles to refine their positions and converge towards the optimal solution.

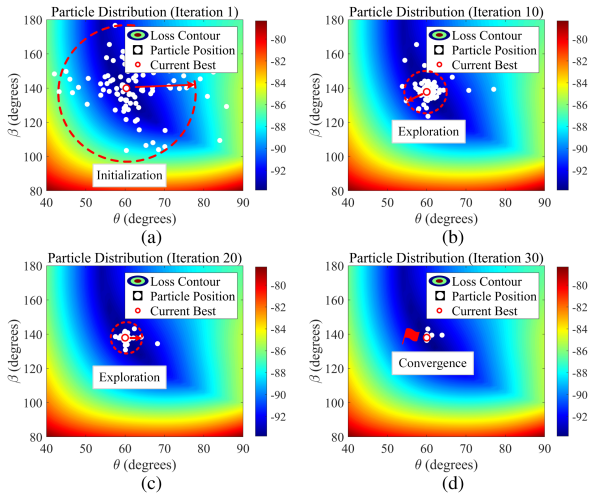

Fig. 7. PSO process for searching the minimum loss, showing particle distribution at different iterations. (a) Initialization phase; (b) Early exploration phase; (c) Late exploration phase; and (d) Convergence phase.

To evaluate the convergence behavior, we conducted 50 independent runs, each capped at 100 iterations. The results indicate that, on average, PSO stabilizes after 30 iterations, with 95% of its optimal value reached within 25 iterations in 90% of cases. The loss function's mean and standard deviation confirm that fluctuations are minor in early iterations, and after 50 iterations, the variance becomes negligible, indicating stable convergence.

These results demonstrate that PSO effectively determines the optimal phase shift angles (θ, β), ensuring both maximum system efficiency and stable power output under varying mutual inductance and load conditions. The next section validates the model and control strategy through experimental deployment and measurement under both fixed and variable coupling conditions.

IV. Experimental Validation Under Fixed Coupling

This section evaluates the proposed control strategy under fixed mutual inductance conditions. All experiments are conducted at a coupling level ($M = 26.52\,\mu H$), with variations applied only to the load resistance R_{L}. The objective is to verify

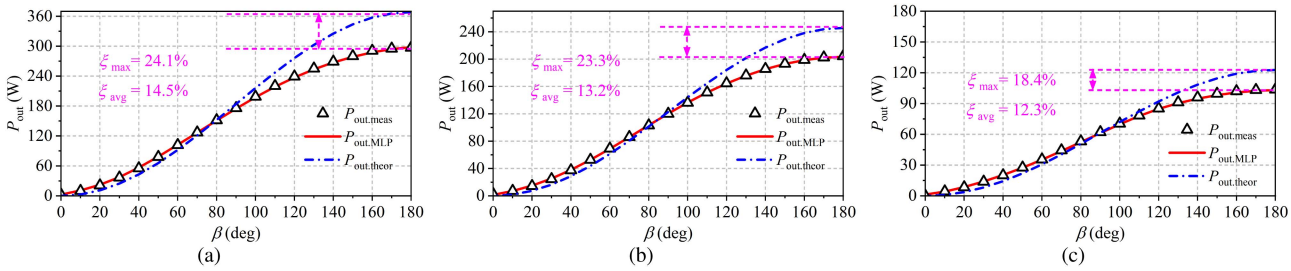

Fig. 8. Comparison of theoretical, measured, and predicted results under fixed $\theta = 90°$ with respect to β: (a) $R_{\mathrm{L}} = 45\,\Omega$; (b) $R_{\mathrm{L}} = 30\,\Omega$; (c) $R_{\mathrm{L}} = 15\,\Omega$.

TABLE II
CONFIGURATION OF MLP FOR OUTPUT MAPPING

Parameter	Description
Selected MLP Inputs	$\theta, \beta, R_{\mathrm{L}}, i_{s\_peak}$
Selected MLP Outputs	P_{o} and η
Hidden Layers	2 layers with 15 and 10 neurons
Activation Function	tanh for hidden layers
MLP Training Configuration	
Training Data (70%)	4763 samples
Validation Data (20%)	1361 samples for structure selection
Testing Data (10%)	680 samples for performance evaluation
Loss Function	Mean Squared Error (MSE)
Optimizer	Levenberg–Marquardt (LM)

TABLE III
PERFORMANCE COMPARISON OF REGRESSION MODELS

Metric	MLP	FHA	RF	SVM
MAPE (P_{o})	0.02097	0.58046	0.10472	0.31055
R^2 (P_{o})	0.9992	0.4430	0.9987	0.9984

key aspects of the framework, including prediction accuracy, optimization effectiveness, deployment feasibility, and system performance under both steady-state and dynamic load conditions. These baseline experiments provide a controlled setting to validate the core functionality of the method before introducing coupling uncertainty in Section V.

A. MLP Modeling Results

To independently model output power P_{o} and efficiency η, two separate MLP networks were developed. This decoupled structure improves prediction accuracy by allowing each network to specialize in learning its respective target, and it also simplifies training, validation, and deployment. While a single multioutput model is theoretically feasible, the two-model setup offers greater flexibility and avoids potential interference between output objectives. (See Table II for MLP configuration.)

In this stage, the mutual inductance M was kept constant during data collection. Consequently, the coupling-related feature i_{s_peak} was treated as a fixed constant and excluded from the model input. The MLP models were therefore trained under a single M condition, focusing on output prediction performance with respect to variations in θ, β, and R_{L} only. This configuration enables evaluation of the model's baseline accuracy before introducing coupling variation in Section V.

These models were compared with traditional FHA and other machine learning models like random forest (RF) and support vector machine (SVM). Table III shows the Mean Absolute Percentage Error (MAPE) and Coefficient of Determination (R^2) for different approaches.

To validate the output prediction algorithm and efficiency optimization strategy, experiments were conducted under various conditions. Fig. 8 shows the variation of output power P_{o} with respect to β for fixed $\theta = 90°$ and load resistances $R = 45\,\Omega$, $30\,\Omega$, and $15\,\Omega$. The comparison between theoretical output power $P_{\mathrm{out,theo}}$ and experimental values $P_{\mathrm{out,expe}}$ reveals negligible mean squared errors (MSE) of 0.316%, 0.216%, and 0.058%, respectively.

The MLP model significantly outperforms FHA, where linear assumptions fail to capture nonlinear system behavior. Theoretical values are derived from the analytical model, while measured values are obtained from experiments, and predicted values come from the MLP-based model. The comparison highlights the MLP model's ability to closely match measured values while capturing deviations from theoretical predictions.

These results demonstrate that the MLP model predicts output power $P_{\mathrm{out,pred}}$ with high accuracy, proving its robustness in predicting system behavior across varying load conditions.

B. PSO Optimization Results

To determine the optimal control parameters (θ, β), offline PSO was performed on a PC for each discrete operating point defined by combinations of load resistance R_{L} and target output power P_{ref}. These optimized solutions are essential for maximizing system efficiency. As shown in Fig. 9, the optimization identifies the optimal combinations of θ and β for different values of R_{L} (45 Ω, 30 Ω, and 15 Ω).

In the 3-D plots, the red dots represent the optimal combinations of θ and β for each P_{o}, reflecting output power levels under different operating conditions.

To enable real-time implementation of the offline-optimized control strategy, two independent ANNs were trained to regress the PSO-generated solutions for θ and β, respectively. This enables smooth control surface representation suitable for real-time deployment.

As shown in Fig. 10, the ANN-based regression achieves excellent performance with MAPE values of 0.71% and 0.28% for efficiency and power output, respectively, and R^2 values of 98.69% and 99.85%. These optimized solutions are then loaded

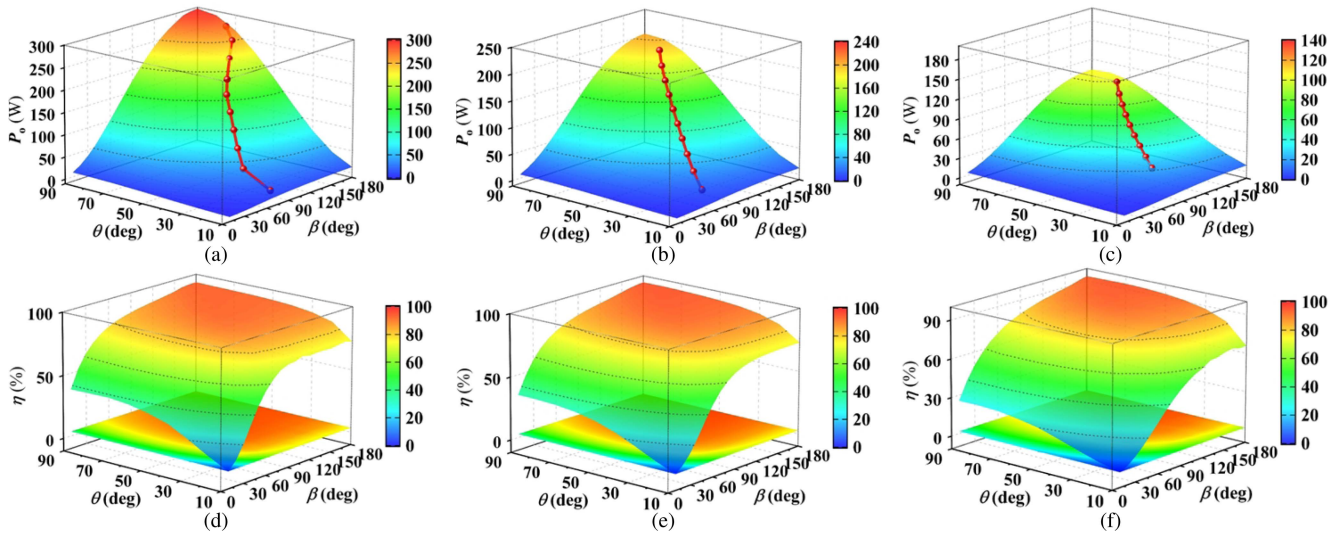

Fig. 9. PSO-based optimization of output power. (a)–(c) Output power P_o and PSO optimization trajectory under $R_L = 45\,\Omega$, $30\,\Omega$, and $15\,\Omega$, respectively. (d)–(f) Corresponding efficiency η distributions.

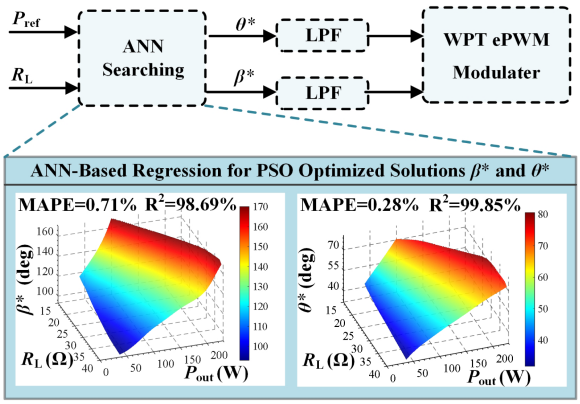

Fig. 10. ANN Regression for PSO-Optimized Switching Parameters β and θ for DSP Implementation.

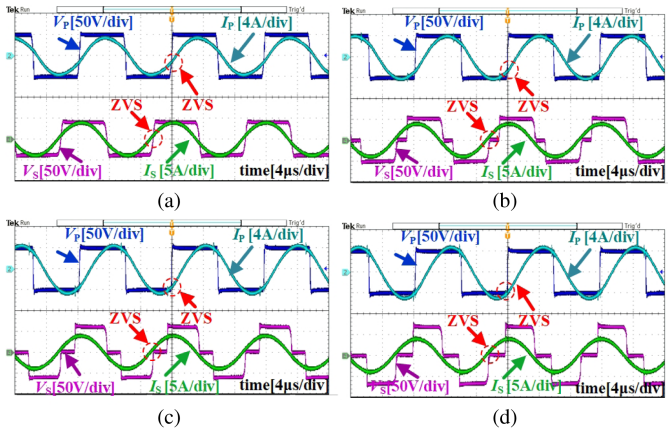

Fig. 11. Steady-state operating waveforms of V_p, I_p, V_s, and I_s at $P_o = 100$ W with R_L = (a) $15\,\Omega$, (b) $25\,\Omega$, (c) $35\,\Omega$, and (d) $45\,\Omega$.

into the DSP for real-time system control, enabling efficient Constant Power (CP) control based on reference power P_{ref} and load resistance R_L. Each ANN has a compact architecture with a single hidden layer of 15 neurons using ReLU activation, and one output neuron. The models are implemented in single-precision floating-point arithmetic and deployed on the TMS320F28335 DSP.

To verify runtime performance, we conducted cycle-level inference timing tests using Code Composer Studio. Each forward inference takes approximately 2645 clock cycles, or 17.6 μs at 150 MHz. This is well within the control period of 35.3 μs (equivalent to 3 PWM cycles at 85 kHz), leaving sufficient timing margin for other tasks such as ADC sampling and protection logic.

The switching behavior on the primary side is implicitly synchronized via the secondary-side current. A zero-crossing detector on the secondary side triggers an interrupt at current zero point, which serves as the timing anchor for executing ANN inference and updating the control angles (θ, β). This interrupt-driven control scheme enables real-time execution without requiring PC-side assistance or bidirectional communication between the primary and secondary controllers. It confirms that the proposed method is both computationally efficient and practically deployable on resource-constrained embedded platforms.

C. Steady-State Results

The steady-state operating waveforms of the inverter and rectifier are shown for different load resistances R_L at $P_o = 100$ W. The waveforms for V_p, I_p, V_s, and I_s are presented under four load conditions: $R_L = 15\,\Omega$, $25\,\Omega$, $35\,\Omega$, and $45\,\Omega$. These waveforms, shown in Fig. 11, demonstrate that zero-voltage switching (ZVS) is achieved across all operating conditions.

The power analyzer results for these operating conditions are shown in Fig. 12. The measured DC input and output voltages,

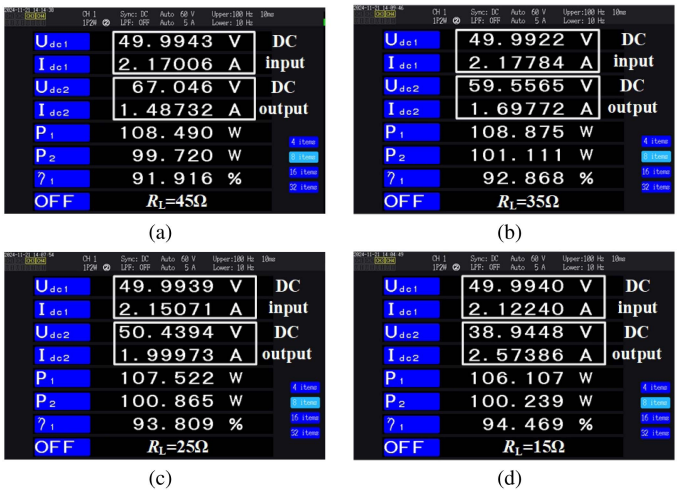

Fig. 12. Power analyzer results at $P_o = 100$ W with $R_L =$ (a) 45 Ω, (b) 35 Ω, (c) 25 Ω, and (d) 15 Ω.

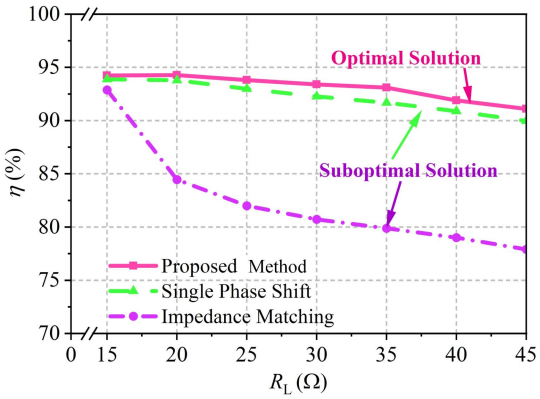

Fig. 13. Efficiency variation with respect to R_L.

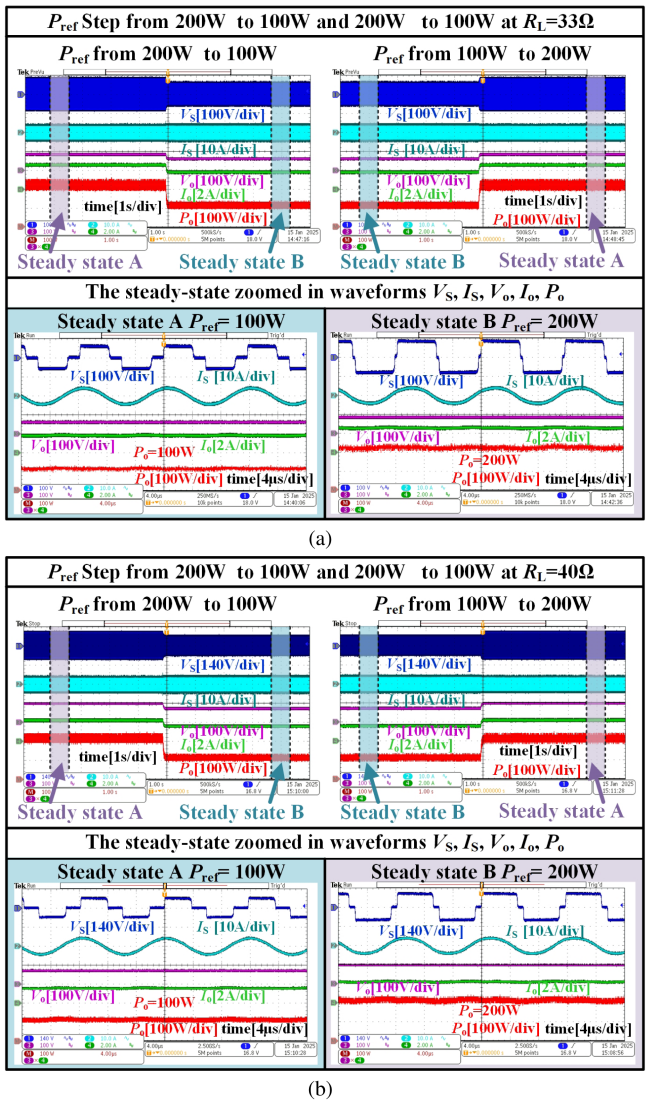

Fig. 14. Steady-state and dynamic waveforms for P_{ref} transition from 100 to 200 W at $R_L =$ (a) 33 Ω and (b) 40 Ω.

along with the power values, indicate that the system operates with high efficiency across all load resistances. The efficiency values for $R_L = 15\,\Omega$, 25 Ω, 35 Ω, and 45 Ω are 94.4%, 93.8%, 92.8%, and 91.9%, respectively, demonstrating the system's robustness across varying load conditions.

Fig. 13 illustrates the variation in efficiency with respect to R_L. As expected for WPT systems, the system's efficiency decreases as the load resistance increases. This result will be compared with existing literature on impedance matching and single-phase shift control, highlighting the proposed system's superior efficiency maintenance across varying load conditions.

D. Transients With Stepping Output Power

The transient response of the system during a step change in reference power P_{ref} from 100 to 200 W is analyzed to evaluate its tracking performance. The results, shown for load resistances $R_L = 33\,\Omega$ and $R_L = 40\,\Omega$, include the top plots depicting the transient response and the bottom plots showing the zoomed-in steady-state waveforms. Fig. 14 illustrates both the transient and steady-state behavior.

For each condition, the waveforms of V_s, I_s, V_o, I_o, and P_o are presented. The top figures illustrate the entire transient process (1 s per grid), highlighting how the system adjusts to the step change in reference power. The bottom figures provide a detailed view of the steady-state operation after the transient response, zoomed in at 4 ms per grid.

The results demonstrate that the system effectively tracks the given power reference and maintains stable operation at both 100 W and 200 W, validating its tracking capability under changing power setpoints.

E. Transients With Stepping Load

The system's transient response was analyzed when the load resistance R_L stepped from 20 to 40 Ω, while maintaining a constant output power of $P_o = 100$ W. The top plots show the dynamic waveforms during the transition, and the bottom plots display the steady-state waveforms after the system stabilizes.

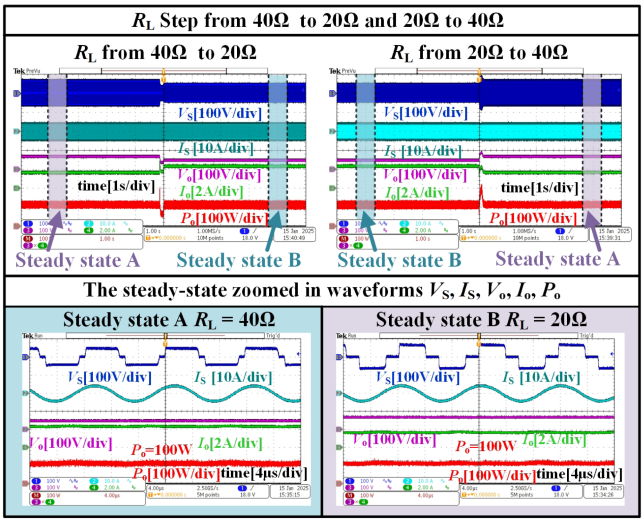

Fig. 15. Steady-state and dynamic waveforms for R_{L} transition from 20 Ω to 40 Ω at constant $P_{\mathrm{o}} = 100$ W.

Fig. 15 shows both the transient and steady-state behavior. The transition from $R_{\mathrm{L}} = 20$ to 40 Ω is captured, with output power P_{o} remaining constant at 100 W. The zoom-in steady-state waveforms illustrate the system's ability to maintain efficient operation even with changes in load resistance, confirming the robustness and reliability of the proposed system.

The results demonstrate that the proposed data-driven modeling and optimization method performs reliably under fixed coupling conditions. To assess its robustness in practical scenarios, the following section presents an extension of the control framework to cope with mutual inductance variations caused by coil misalignment.

V. Control Generalization Under Misalignment

In practical WPT applications, coil misalignment and load variation often occur simultaneously, affecting mutual inductance M and load resistance R_{L}, respectively. These variations can significantly impact output power and system efficiency. To evaluate the adaptability of the proposed framework under such conditions, this section presents a generalized control strategy that extends the models used in Section IV. Specifically, the secondary current peak i_{s_peak} is introduced as an additional input feature to capture real-time changes in coupling conditions caused by lateral misalignment. The new input set $(R_{\mathrm{L}}, P_{\mathrm{ref}}, i_{s\_peak})$ is used throughout the workflow, including data collection, MLP-based modeling, PSO optimization, and ANN regression.

It is important to note that the control models used here are structurally similar to those in Section IV, but trained separately with the expanded input feature set. This allows the system to respond effectively to both coupling and load disturbances without measuring mutual inductance M, while also demonstrating the extensibility of the proposed framework. The following subsections describe the experimental setup under misalignment, model adaptation, and real-time performance evaluation under varied coupling and loading conditions.

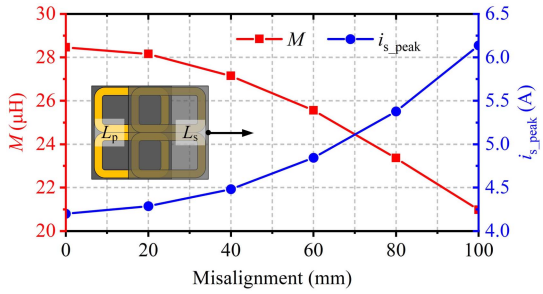

Fig. 16. Variation of M and i_{s_peak} under lateral coil misalignment.

A. Experimental Setup Under Misalignment

To evaluate the control strategy under realistic conditions involving simultaneous coupling and load variation, additional experiments with deliberate coil misalignment were carried out. The receiver coil was laterally displaced from 0 to 10 cm in 2 cm increments, simulating installation deviations commonly encountered in practice.

Each offset level corresponds to a specific mutual inductance M, decreasing from 28.46 μH (aligned) to 20.98 μH (maximum offset). The secondary current peak i_{s_peak} serves as a real-time observable that reflects changes in mutual inductance, avoiding the need to directly measure mutual inductance M. The correlation between mutual inductance M and the secondary current peak i_{s_peak} is characterized by the analytical relationship previously defined in (7). The variation of mutual inductance and its corresponding secondary current peak values under different misalignment conditions is illustrated in Fig. 16.

In the extended framework, i_{s_peak} is used directly as input to both the MLP, PSO, and ANN models. This allows the control system to adapt to changes in coil alignment based solely on local current measurements. For each displacement, the control parameter space $(\theta, \beta, R_{\mathrm{L}})$ was scanned in the same way as in the baseline experiment. The expanded dataset was then used to train updated prediction and control models.

The measured variations of mutual inductance M and corresponding i_{s_peak} values are plotted in Fig. 16. The monotonic and smooth trends confirm that i_{s_peak} can reliably track coupling changes and supports the feasibility of generalized control.

B. MLP-Based Prediction Under Misalignment

To evaluate the generalization ability of the MLP-based prediction model under varying coupling conditions, a leave-one-mutual-inductance-out validation strategy was employed. Specifically, the dataset corresponding to a particular mutual inductance value was excluded during training and used solely for testing. This setting emulates deployment in unseen misalignment scenarios and tests the model's ability to interpolate across coupling levels.

As an example, the dataset corresponding to $M = 23.36\,\mu H$ was reserved for testing, while all other M levels were included

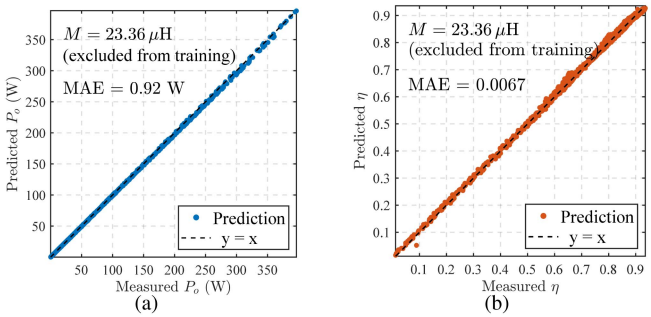

Fig. 17. Prediction accuracy of the MLP model on the excluded coupling case with $M = 23.36\,\mu$H: (a) output power P_o; (b) efficiency η.

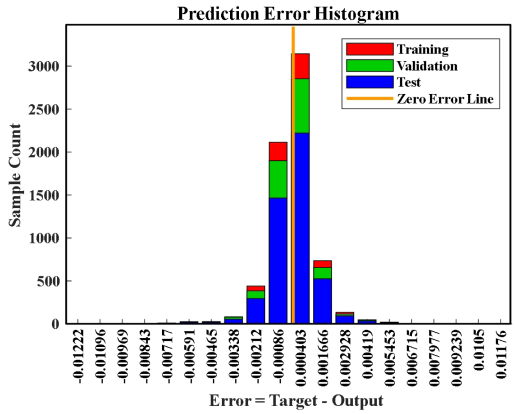

Fig. 18. Prediction error histogram of the MLP model for training, validation, and test datasets.

in the training and validation sets. The MLP was trained using the extended input set $(\theta, \beta, R_L, i_{s\_peak})$ and tasked with predicting the output power P_o and efficiency η under the excluded condition. The predicted versus measured results for P_o and η are shown in Fig. 17, which demonstrates excellent agreement. Fig. 17(a) presents the predicted and actual output power P_o, while Fig. 17(b) shows the corresponding efficiency η. Both subplots highlight the model's ability to accurately track the system response under unseen coupling conditions, validating its generalization capability.

To further validate the reliability of the MLP under coupling variation, Fig. 18 presents the prediction error histogram across all data subsets. The residuals are tightly clustered around zero, and no significant skew or outliers are observed. This confirms that the model maintains low-bias and consistent performance.

C. ANN Regression and Control Deployment Under Misalignment

Based on the extended dataset incorporating mutual inductance variation, a new set of PSO optimization runs was performed to determine the optimal switching parameters (θ^*, β^*) for different combinations of system conditions. The optimization was conducted over a three-dimensional input space, where the load resistance was set as $R_L = 15 : 2 : 45\,\Omega$, the target output power as $P_{ref} = 50 : 20 : 350$ W, and the secondary current

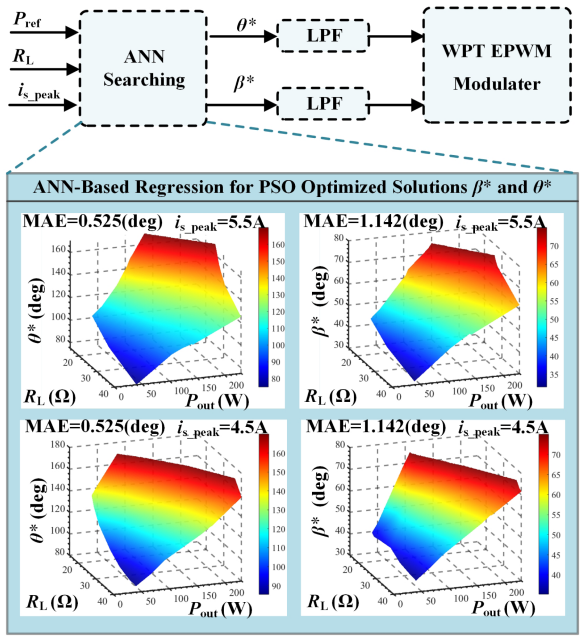

Fig. 19. ANN Regression for PSO-Optimized Switching Parameters β and θ for DSP Implementation.

peak as $i_{s\_peak} = 4.0 : 0.2 : 6.2$ A. This configuration resulted in a total of 3,072 discrete operating points, each representing a unique combination of coupling and loading conditions. PSO was used offline at each point to determine the corresponding optimal switching angles.

To enable real-time implementation, two lightweight ANNs were trained to regress the optimal θ^* and β^* values from the input set $(R_L, P_{ref}, i_{s\_peak})$. Each ANN consists of a single hidden layer with 15 ReLU-activated neurons and one linear output neuron. This design achieves a balance between regression accuracy and computational efficiency.

The regression results are shown in Fig. 19, demonstrating smooth, continuous control surfaces over the full range of operating conditions. The ANN outputs closely follow the PSO-optimized values, with mean absolute errors (MAE) below 1.142°. The trained ANNs were installed on a TMS320F28335 DSP using the MATLAB Coder. Each inference takes approximately 2645 clock cycles, or 17.6 μs at 150 MHz, well within the 35.3 μs (three cycles for 85 kHz) control period. During operation, the DSP receives real-time measurements of R_L, P_{ref}, i_{s_peak}, and directly computes θ^* and β^* for control.

D. Experimental Validation Under Misalignment

To verify the effectiveness of the generalized control strategy under practical conditions, experiments were performed using the ANN-based controller deployed on the DSP. The system was tested in 9 combinations of mutual inductance M and load resistance R_L, covering three coupling levels $(28.46\,\mu H,\ 25.56\,\mu H,\ 20.98\,\mu H)$ and three load values $(20\,\Omega,\ 30\,\Omega,\ 40\,\Omega)$. The target output power P_{ref} was fixed at 100 W in all cases.

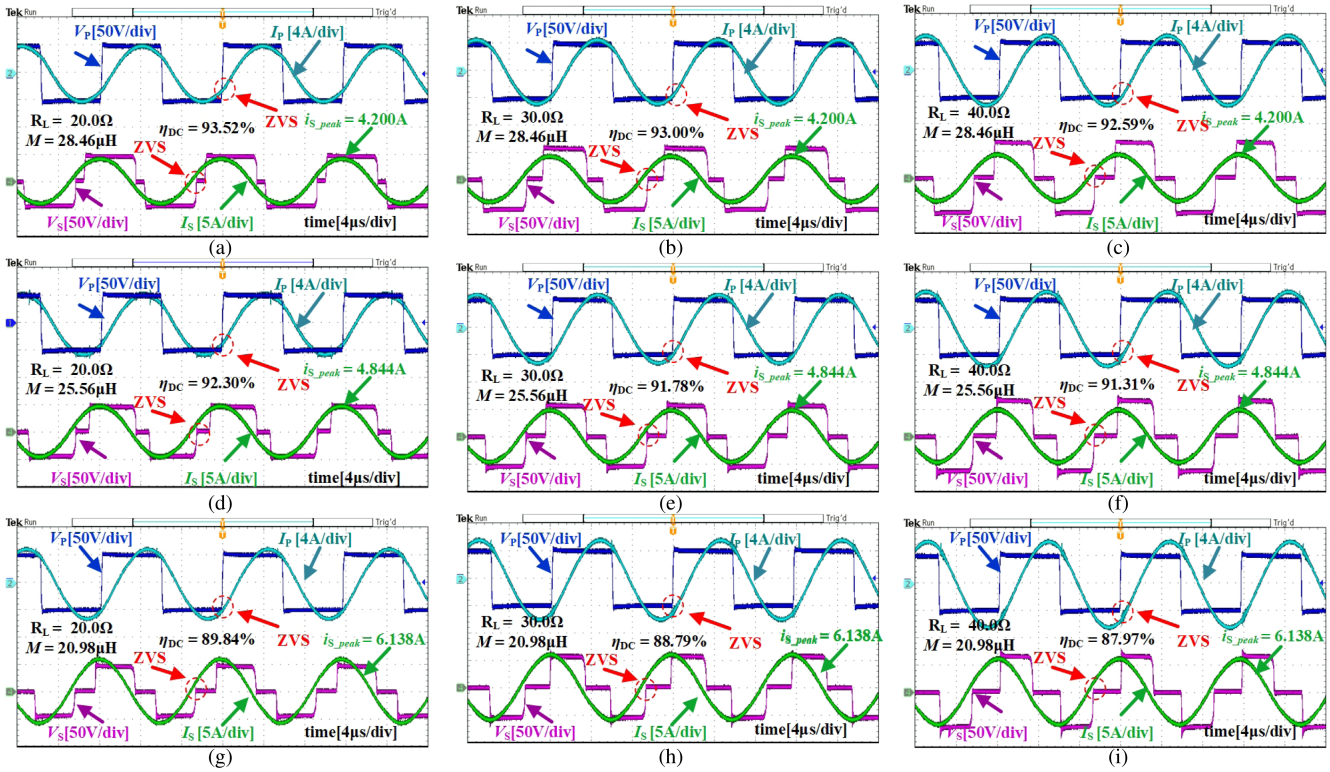

Fig. 20. Measured waveforms at $P_o = 100$ W under varying load resistances R_L (columns: 20 Ω, 30 Ω, 40 Ω) and mutual inductances M (rows: 28.46 μH, 25.56 μH, 20.98 μH). (a) {20Ω, 28.46μH}; (b) {30Ω, 28.46μH}; (c) {40Ω, 28.46μH}; (d) {20Ω, 25.56μH}; (e) {30Ω, 25.56μH}; (f) {40Ω, 25.56μH}; (g) {20Ω, 20.98μH}; (h) {30Ω, 20.98μH}; and (i) {40Ω, 20.98μH}

The measured waveforms are shown in Fig. 20, covering all test conditions. For each test, the controller received real-time inputs $(R_L, P_{ref}, i_{s\_peak})$, inferred the optimal switching parameters (θ^*, β^*), and applied them via the DSP. The resulting inverter voltage and current waveforms, as well as secondary side responses, were captured to evaluate steady-state performance and switching behavior. In each case, the system maintains stable output power, clean switching transitions, and clear ZVS characteristics. Across all operating points, the measured system efficiency remains above 87.9%, with a peak value of 93.52%.

These results demonstrate that the proposed data-driven controller retains performance robustness even under significant physical variation, validating its applicability to real-world deployment scenarios where precise coil alignment cannot be guaranteed. While the controller maintains consistent power output across all test conditions, slight differences in measured efficiency between Section IV and Section V were observed. These differences fall within an acceptable range and do not affect the overall control accuracy. The stability of P_o across varying operating points further confirms the reliability and repeatability of the proposed framework.

E. Computation Cost and Deployment Efficiency

To complement the experimental validation, a detailed analysis of the computation time for each stage of the proposed control framework is provided in Table IV. This breakdown highlights the distinction between offline operations (used during MLP training and PSO control surface generation) and online execution deployed on the embedded controller.

TABLE IV
COMPUTATION TIME FOR EACH STAGE

Items	MLP Prediction	PSO Optimization	ANN Deployment
Inference time	2.86 μs (per point)	–	2645 cycles (17.6 μs)
Total time	train 32.5 s (6804 points)	6 h 11 min (offline)	train 8.5 s (full sweep)

The MLP model is used offline to regress output power and efficiency across the parameter space, taking approximately 32.5 s to process all 6804 operating points. The PSO optimization stage, while more computationally intensive, is executed only once and requires approximately 6 h to generate the full control dataset.

In contrast, the ANN inference is executed in real time on the DSP. Each inference takes approximately 2645 clock cycles in 150 MHz (17.6 μs), allowing the control updates to complete well within the 35.3 μs control period (3 PWM cycles).

These results demonstrate that the proposed method achieves a strong balance between offline modeling flexibility and

real-time deployability. The lightweight nature of the ANN-based controller ensures compatibility with low-cost embedded platforms.

VI. Conclusion

Traditional methods for optimizing system efficiency are constrained by model complexity and calculation accuracy. In this article, a novel data-driven efficiency optimization method for WPT systems has been proposed by integrating MLP and PSO, which is initially configured to accurately capture the relationship between control inputs and system performance. To enable real-time deployment, the PSO-optimized control surfaces are regressed using compact ANNs and implemented into microcontrollers, with each completing inference of 17.6 μs. Furthermore, this method is suitable for WPT scenarios, i.e., where R_{L} and M vary simultaneously. Experimental results validate that the maximum mean absolute percentage error (MAPE) in prediction is 3.5%, while the system efficiency remains above 87.97%, reaching a peak value of 94.4%. Consequently, this study provides a promising and practical solution for enhancing the efficiency of WPT systems in real-world scenarios.

References

[1] Z. Zhang, H. Pang, A. Georgiadis, and C. Cecati, "Wireless power transfer—an overview," *IEEE Trans. Ind. Electron.*, vol. 66, no. 2, pp. 1044–1058, Feb. 2019.

[2] A. Aktas, O. C. Onar, E. Asa, M. Mohammad, B. Ozpineci, and L. M. Tolbert, "Sensitivity analysis of a polyphase wireless power transfer system under off-nominal conditions," *IEEE Trans. Transp. Electrific.*, vol. 10, no. 3, pp. 6690–6706, Sep. 2024.

[3] C. Xia et al., "Dual-frequency metal object detection based on SPWM control for wireless EV charging system," *IEEE Trans. Power Electron.*, vol. 40, no. 1, pp. 2604–2618, Jan. 2025.

[4] B. Zhang, C. Q. Jiang, F. Yang, C. Chen, Y. Lu, and J. Zhou, "An antirotation wireless power transfer system with a flexible magnetic coupler for autonomous underwater vehicles," *IEEE Trans. Power Electron.*, vol. 40, no. 1, pp. 2593–2603, Jan. 2025.

[5] Z. Chen, X. Zhang, F. Xu, M. Li, Z. Yuan, and Q. Yang, "Wide rotation-misalignment-tolerance design of magnetic coupled structure for AUVs wireless charging system," *IEEE Trans. Ind. Electron.*, vol. 71, no. 11, pp. 14086–14096, Nov. 2024.

[6] C. R. Teeneti, T. T. Truscott, D. N. Beal, and Z. Pantic, "Review of wireless charging systems for autonomous underwater vehicles," *IEEE J. Ocean. Eng.*, vol. 46, no. 1, pp. 68–87, Jan. 2021.

[7] Q. Huang, Z. Ma, S. Wang, and Y. Yang, "Integration of near-field communication (NFC) antenna and wireless charging coil for portable electronic products," *IEEE J. Emerg. Sel. Topics Power Electron.*, vol. 12, no. 4, pp. 3415–3425, Aug. 2024.

[8] W. X. Zhong and S. Y. R. Hui, "Maximum energy efficiency tracking for wireless power transfer systems," *IEEE Trans. Power Electron.*, vol. 30, no. 7, pp. 4025–4034, Jul. 2015.

[9] Z. Shen, C. Liu, H. Tang, X. Chen, and Y. Zhang, "A misalignment-insensitive hybrid reconfigurable wireless charging system for constant-voltage and constant-current outputs based on a novel bipolar coil symmetrical to two perpendicular directions," *IEEE Trans. Power Electron.*, vol. 39, no. 12, pp. 16904–16915, Dec. 2024.

[10] C. Ma, X. Qu, J. Liu, and L. Tan, "A novel cascaded buck active rectifier with arbitrary impedance conversion ratio for inductive power transfer system," *IEEE Trans. Transp. Electrific.*, vol. 10, no. 4, pp. 9478–9489, Dec. 2024.

[11] S. Liu, Y. Feng, W. Weng, Y. Lin, J. Wu, and X. He, "Contactless-sensor-based output feedback control with maximum efficiency tracking technique in inductive power transfer systems," *IEEE Trans. Power Electron.*, vol. 38, no. 7, pp. 9218–9229, Jul. 2023.

[12] S. Nie, W. Han, Z. Luo, C. Perera, and P. W. Lehn, "Sequential mutual-inductance identification method for wireless power transfer systems of electric vehicles," *IEEE Trans. Transp. Electrific.*, vol. 10, no. 3, pp. 5178–5189, Sep. 2024.

[13] S. Niu, R. Lyu, J. Lyu, K. T. Chau, W. Liu, and L. Jian, "Optimal resonant condition for maximum output power in tightly coupled WPT systems considering harmonics," *IEEE Trans. Power Electron.*, vol. 40, no. 1, pp. 152–156, Jan. 2025.

[14] Z. Zhang et al., "A dynamic wireless power transfer system using DC-controlled variable inductor for segment transmitter automatic switching," *IEEE Trans. Power Electron.*, vol. 40, no. 1, pp. 23–27, Jan. 2025.

[15] S. Li, F. Li, R. Zhang, C. Tao, and L. Wang, "Accurate modeling, design, and load estimation of LCC-S based WPT system with a wide range of load," *IEEE Trans. Power Electron.*, vol. 38, no. 10, pp. 11763–11775, Oct. 2023.

[16] Y. Guo, Y. Zhang, W. Zhang, and L. Wang, "Battery parameter identification based on wireless power transfer system with rectifier load," *IEEE Trans. Ind. Electron.*, vol. 68, no. 8, pp. 6893–6904, Aug. 2021.

[17] F. Xu, S. C. Wong, and C. K. Tse, "Overall loss compensation and optimization control in single-stage inductive power transfer converter delivering constant power," *IEEE Trans. Power Electron.*, vol. 37, no. 1, pp. 1146–1158, Jan. 2022.

[18] J. Jiang, K. Song, Z. Li, C. Zhu, and Q. Zhang, "System modeling and switching control strategy of wireless power transfer system," *IEEE J. Emerg. Sel. Topics Power Electron.*, vol. 6, no. 3, pp. 1295–1305, Sep. 2018.

[19] F. Xu, S.-C. Wong, and C. K. Tse, "Inductive power transfer system with maximum efficiency tracking control and real-time mutual inductance estimation," *IEEE Trans. Power Electron.*, vol. 37, no. 5, pp. 6156–6167, May 2022.

[20] Z. Xiao et al., "A hybrid data-driven power loss minimization method of dual-active bridge converters," *IEEE Trans. Power Electron.*, vol. 39, no. 5, pp. 5820–5832, May 2024.

[21] X. Li, X. Zhang, F. Lin, C. Sun, and K. Mao, "Artificial-intelligence-based triple phase shift modulation for dual active bridge converter with minimized current stress," *IEEE J. Emerg. Sel. Topics Power Electron.*, vol. 11, no. 4, pp. 4430–4441, Aug. 2023.

[22] Y. Wu et al., "Precise coil inductance prediction in WPT systems: A transfer learning approach," *IEEE Trans. Transp. Electrific.*, vol. 11, no. 2, pp. 7083–7095, Apr. 2025.

[23] K. Wang, Y. Yang, and X. Zhang, "Advanced front-end monitoring scheme for inductive power transfer systems based on random forest regression," in *Proc. IEEE Appl. Power Electron. Conf. Expo.*, Orlando, FL, USA, 2023, pp. 2901–2907.

Fei Xu (Member, IEEE) received the B.Eng. degree in electrical engineering from China Agricultural University, Beijing, China, in 2016, the M.Phil. degrees in electrical engineering from the Institute of Electrical Engineering, Chinese Academy of Sciences, Beijing, in 2019, and the Ph.D. degree in power electronics from The Hong Kong Polytechnic University, Hong Kong, in 2022.

He is currently an Assistant Professor with the Department of Electrical Engineering and the State Key Laboratory of Intelligent Power Distribution Equipment and System, Hebei University of Technology, Tianjin, China. His research interests include wireless power transfer, power electronic, and electric vehicles.

Xiquan Deng was born in Hebei, China, in 2002. He received the B.S. degree in electrical engineering, in 2023, from the Hebei University of Technology, Tianjin, China, where he is currently working toward the M.S. degree in electrical engineering.

His current research interests include wireless power transfer, modulation design, and application of artificial intelligence in power electronics.

Zhixin Chen (Graduate Student Member, IEEE) received the B.S. degree in electrical engineering and automation from Liren College of Yanshan University, Qinhuang-dao, China, in 2018, and the M.S. degree in electrical engineering in 2022 from the Tiangong University, Tianjin, China. He is currently working toward the Ph.D. degree in electrical engineering from the Hebei University of Technology, Tianjin, China.

His current research interests include wireless power transfer, and its industrial applications.

Xian Zhang received the M.E. and Ph.D. degrees in electrical engineering from the Hebei University of Technology, Tianjin, China, in 2009 and 2012, respectively.

He is currently a Professor with the Hebei University of Technology. He is the Director of the China Electrotechnical Society and the Secretary General of the National Specialized Committee on Wireless Power Transmission Technology. His research interests encompass intelligent high power wireless power transmission technology, measurement of 3-D electromagnetic fields, and numerical calculations of modern engineering electromagnetic fields.

Chi K. Tse (Fellow, IEEE) received the B.Eng. degree (Hons.) with first class honors in electrical engineering and the Ph.D. degree in electrical engineering from the University of Melbourne, Australia, in 1987 and 1991, respectively.

He is currently Associate Vice President (Innovation), Director of Academy of Innovation, and Chair Professor of Electrical Engineering with the City University of Hong Kong, Hong Kong. His research interests include power electronics, nonlinear systems and complex network applications.

Dr. Tse was the recipient of the 2019 Silicon Valley Invention Grand Prize/Gold Medal, 2022 IEEE CASS Desoer Technical Achievement Award, and multiple IEEE /Journal Best Paper Awards. He holds distinguished titles such as Chang Jiang Scholar Chair Professor at Huazhong University of Science and Technology, Honorary Professor of the University of Melbourne, and Distinguished Professor at-Large at the University of Western Australia. He was selected as three-time IEEE Distinguished Lecturer (2005/2010/2018). He chaired the IEEE CAS Nonlinear Circuits Committee (2006). He serves and has served as Editor-in-Chief for IEEE TRANSACTIONS ON CIRCUITS AND SYSTEMS II (2016–2019), *IEICE Nonlinear Theory and Applications* (since 2013); and on the Editorial Board of IEEE Proceedings (2021–2024). He served on IEEE committees (Fellows, Awards, IEEE Trans. Netw. Sci. Eng Steering) and advisory roles at Hong Kong Research Grants Council and government committees.